C. R. Mecanique 346 (2018) 964–977

Contents lists available at ScienceDirect

Comptes Rendus Mecanique

www.sciencedirect.com

Jet noise modelling and control / Modélisation et contrôle du bruit de jet

Large eddy simulation of serration effects on an ultra-high-bypass-ratio engine exhaust jet

Zhong-Nan Wang *, James Tyacke, Paul Tucker

Department of Engineering, University of Cambridge, Cambridge CB2 1PZ, UK

ARTICLE INFO

Article history:
Received 30 July 2017
Accepted 9 April 2018
Available online 16 August 2018

Keywords:
Large-eddy simulation
Ultra-high bypass-ratio (UHBPR) engine
Noise reduction
Serrated nozzle

ABSTRACT

Serrated jet nozzles are considered to be an efficient and practical passive control approach for jet noise. However, some fundamental mechanisms of serration effects on jet noise are not fully understood, especially in terms of the sound source. In this paper, a high-fidelity simulation framework using large-eddy simulation (LES) is demonstrated to predict near-field turbulence and far-field acoustics from an ultra-high-bypass-ratio engine with round and serrated nozzles. Far-field sound is predicted using Ffowcs Willams–Hawkings (FWH) integration. The results show that the serrated nozzle increases mixing near the nozzle and hence the turbulence decay rate, reducing the turbulence level downstream. The serrations shift the energy from the low frequencies to the high frequencies and decrease overall sound pressure levels by about 3 dB over the low-frequency range. Sound sources are analysed based on fourth-order space–time correlations. There are six major source components (R_{1111}, R_{2222}, R_{3333}, R_{1313}, R_{1212}, and R_{2323}) inside the jet shear layers. The serrations are able to reduce the amplitude of these source terms, causing them to decay rapidly to a level below the round nozzle jet within $2D$ downstream of the nozzle.

1. Introduction

Aircraft noise has become a major concern to residents neighbouring airports nowadays as the air traffic volume is increasing dramatically. Among aircraft noise sources, jet noise is the dominant component when an aircraft takes off. Research about the jet noise dates back to Lighthill and his celebrated eighth power law [1]. Since then, considerable progress has been made in this field, but the main noise reduction technology still follows the guidance of Lighthill's theory and relies mainly on reducing the exhaust exit velocity by aeroengine bypass ratio increase [2]. Some current research shows that noise reduction can be achieved by altering the flow structures responsible for sound generation without substantially reducing the exhaust velocity [3] and this concept can be accomplished through active and passive control [4]. Therefore, more insight into jet turbulence and its effects on sound sources is needed to explore the potential of noise-control strategies.

Noise control strategies are considered if it is not practical to increase the bypass ratio any further. For example, engines become so large in diameter that there is little room between the engine and the ground or wing. Nozzle serrations are regarded as an effective noise control technology without bypass ratio increase and has been successfully used on several civil aeroengines. Research into the effects of nozzle serrations on jet noise was first focused on isolated jets [5–7]. It shows

* Corresponding author.
E-mail address: znw22@cam.ac.uk (Z.-N. Wang).

https://doi.org/10.1016/j.crme.2018.07.003
1631-0721/

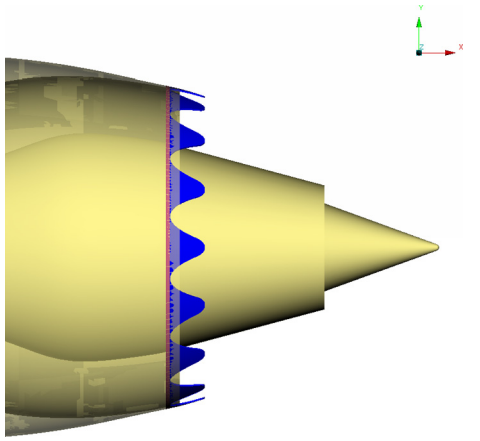

Fig. 1. Overlay of baseline and serrated nozzle geometries.

Table 1
Jet operating conditions.

	p_0/p_a	T_0/T_a	$\dot{m}$ (kg/s)
Bypass	1.342	1.128	6.373
Core	1.222	2.652	0.414

that the serrations can break down large coherent flow structures and reduce the isolated jet noise at low polar angles. Mengle [8,9] tried to design azimuthally varying chevrons (serrations) to reduce the installation noise generated when the jet is mounted to the airframe and test them experimentally. However, due to the lack of detailed unsteady flow data, the serration effects have not been fully understood and the design of serrations mainly relies on empirical experience gained from a range of limited rig tests.

Large-eddy simulation (LES) is a reliable method to capture the flow structures that are responsible for sound generation. Compared to the experiments, it can provide much more insight into the unsteady flow field and reveal the sound source mechanisms. It has proved to be a reliable predictive tool for jet noise [10] and has been successfully used to simulate single-stream round [11,12] and serrated nozzle jets [13] and coaxial dual-stream jets [14,15]. In this paper, an LES framework is demonstrated to simulate an ultra-high bypass-ratio (UHBPR) jet engine with and without serrations. The paper explores the serration effects on the jet flow, acoustics, and its sources using the LES data. It also shows its potential and mechanism to reduce jet noise in the circumstance of UHBPR aeroengines. The article is organized into three parts: first, the simulated cases are introduced. Then the simulation methodology is shown, describing LES methods and a modular hybrid mesh strategy for serrated nozzles. Finally, the LES results are analysed from the perspectives of jet aerodynamics and acoustics.

2. Case description

The simulation is performed for an UHBPR jet. Two cases are numerically simulated in this paper to investigate the serration effects. One is the baseline round nozzle, the other is the serrated nozzle. Fig. 1 shows the overlap of two nozzle geometries. The serrations are shown in blue and the baseline nozzle in pale yellow. Sixteen serrations are designed around the bypass nozzle edge to increase near-nozzle mixing. The serration roots are set slightly backward compared to the baseline nozzle lip; however the tips protrude further downstream. This is to reduce the serration penalties on nozzle performance. The bypass and core mass flow remain unaltered. The two nozzles are operating at the same condition and under an outer flight stream of 90 m/s. The nozzle operating conditions are summarized in Table 1. The corresponding Reynolds and Mach numbers based on bypass velocity and nozzle diameter are 3×10^6 and 0.66. The bypass ratio of the nozzle is around 15, which is representative of UHBPR engines. By comparing these two cases, the serration effects can be quantified.

3. Methodology

To predict this flow, LES is used to simulate large turbulent structures in the jet plume and RANS to model streaks in the attached boundary layers on the nozzle. The methodology, including turbulence modelling, serrated nozzle meshing strategy, and far-field sound prediction, are introduced as follows.

3.1. Hybrid LES-RANS turbulence modelling

The solver used here is an edged-based finite volume code. The compressible flow equations are solved in the discretized integral form.

$$\Omega_i \frac{\partial U_i}{\partial t} = \sum_{j \in E(i)} (F_{ij}^{\mathrm{v,n}} - F_{ij}^{\mathrm{c,n}}) S_{ij}^{\mathrm{n}} \tag{1}$$

where the subscript i represents in the mesh element i and ij represents the control surface between the mesh elements i and j. The superscript 'n' represents the surface normal direction pointing outwards the control volume. $E(i)$ is the set of elements neighbouring the element i. Ω is the volume of the mesh element. U represents the conservative variables $[\rho, \rho\vec{u}, \rho E]$, $F^{\mathrm{v,n}}$ represents surface-normal viscous fluxes $[0, \vec{\tau}^{\mathrm{n}}, \vec{\tau}^{\mathrm{n}} \cdot \vec{u} - q^{\mathrm{n}}]$, and $F^{\mathrm{c,n}}$ represents convective fluxes $[\rho u^{\mathrm{n}}, \rho\vec{u}u^{\mathrm{n}} + p\vec{\mathrm{n}}, \rho H u^{\mathrm{n}}]$. ρ, u, E, H, τ, and q are flow density, velocity, total internal energy, total enthalpy, viscous stress, and heat conduction, respectively.

In LES, around 90 percent of turbulence kinetic energy needs to be resolved and this requires non-dissipative high-resolution numerical schemes. In this study, a non-dissipative numerical method is utilised to preserve kinetic energy [16] and has been shown to correctly predict the turbulence energy cascade [14,17]. The numerical convective flux contains two parts and can be written as

$$F_{ij}^{\mathrm{c,n}} = F_{ij,\mathrm{KEP}}^{\mathrm{n}} - \frac{1}{2}\varepsilon |A_{ij}^{\mathrm{c,n}}| [L(U_j) - L(U_i)] \tag{2}$$

where, $F_{ij,\mathrm{KEP}}^{\mathrm{n}}$ is the kinetic energy preserving fluxes $[\bar{\rho}\bar{u}^{\mathrm{n}}, \bar{\rho}\vec{\bar{u}}\bar{u}^{\mathrm{n}} + \bar{p}\vec{\mathrm{n}}, \bar{\rho}\bar{H}\bar{u}^{\mathrm{n}}]$, the overbar is the arithmetic averaging operator using the values in the adjacent mesh elements i and j. $A_{ij}^{\mathrm{c,n}}$ is the surface-normal Jacobian matrix $\frac{\partial F_{ij}^{\mathrm{c,n}}}{\partial U}$, L is the Laplacian operator $\frac{\partial^2}{\partial x_k x_k}$. The parameter ε controls artificial dissipation level in the simulation.

The first part of this flux is the non-dissipative kinetic energy-preserving scheme and has low sensitivity to grid cell types, allowing a range of mesh topologies to be utilised. It is designed to perform LES with low dissipation. The second part is numerical smoothing. This is used to provide the sponge region towards the computation domain boundary and stabilize the computation. The viscous fluxes $F_{ij}^{\mathrm{v,n}}$ are calculated using the central difference method. The time derivatives $\frac{\partial U_i}{\partial t}$ are discretized by the second-order backward Euler scheme and coupled with dual time stepping for unsteady simulations.

To avoid the severe cost of resolving near-wall streaks at the high Reynolds number considered ($Re = \frac{U_{\mathrm{flight}} D_{\mathrm{bypass}}}{\nu} = 2 \times 10^6$), RANS layer are used to model the boundary layers on the nozzle surfaces. The RANS layer is blended with the LES region based on a modified wall distance [18]. The blending is achieved at the stress level, the Spalart–Allmaras (SA) RANS model stresses [19] are hybridized with non-linear SGS stresses [20]. The hybrid turbulence model stress is expressed as

$$\tau_{ij}^{\mathrm{model}} = \bar{L} + \overline{NL} \tag{3}$$

where $\bar{L}$ and $\overline{NL}$ represent the linear and non-linear parts, respectively, of the modelled turbulence stress. The blended linear and nonlinear stress terms are

$$\bar{L} = \frac{\tau_{kk}\delta_{ij}}{3} + 2[f \cdot \mu_{\mathrm{SGS}} + (1-f) \cdot \mu_{\mathrm{RANS}}] S_{ij} \tag{4}$$

$$\overline{NL} = \rho C_\alpha \Delta^2 f \left(\frac{\partial u_i}{\partial x_l}\frac{\partial u_l}{\partial x_j} + \frac{\partial u_i}{\partial x_l}\frac{\partial u_j}{\partial x_l} + \frac{\partial u_l}{\partial x_i}\frac{\partial u_l}{\partial x_j}\right) \tag{5}$$

where $S_{ij} = 0.5(\partial u_i/\partial x_j + \partial u_j/\partial x_i)$ is the strain rate tensor, $\Delta = vol^{1/3}$ is the filter length. The blending function f is based on the wall distance d, which becomes one in the LES region.

$$f(d) = \min[\max(\frac{d - (1-\beta)\, d_{\mathrm{RANS}}}{\beta\ d_{\mathrm{RANS}}}, 0), 1] \tag{6}$$

d_{RANS} represents the specified RANS layer thickness, and β defines the size of RANS-to-LES transition zone. The blending function is shown with the computed SA RANS variable in Fig. 2.

Far-field characteristic free-stream boundary conditions are set at the side and flight-inlet boundaries. Static pressure is set at the outlet boundary and total pressure and total temperature at the core and bypass duct inlet. To reduce the numerical reflection, high-dissipative sponge regions are place near the computational boundaries. Turbulence is triggered naturally by Kelvin–Helmholtz instability using turbulent boundary profile from RANS layer near the nozzle wall and transition happens immediately within half diameter downstream the nozzle. The simulation is collected for around 200 $D_{\mathrm{bypass}}/U_{\mathrm{bypass}}$ time units for statistics and spectra calculation. As estimated in [14], the cost of this type simulation can be € 13–18 k for the current grid scale, while the typical jet noise rig testing costs around € 200 k.

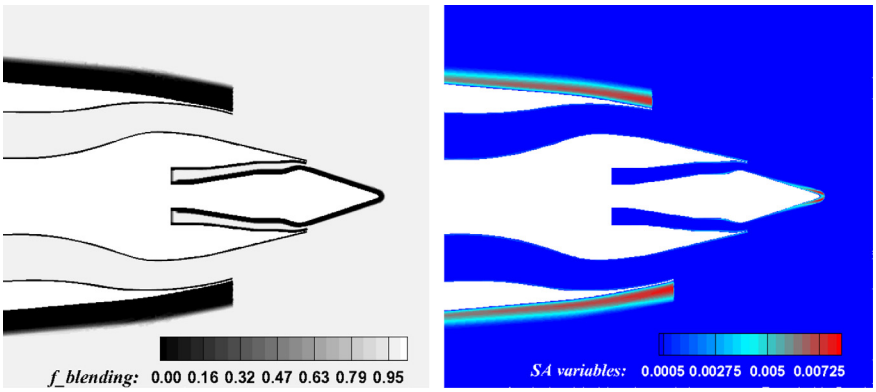

(a) Blending function f (b) SA variable

Fig. 2. Interactions between the jet and the wing/flap.

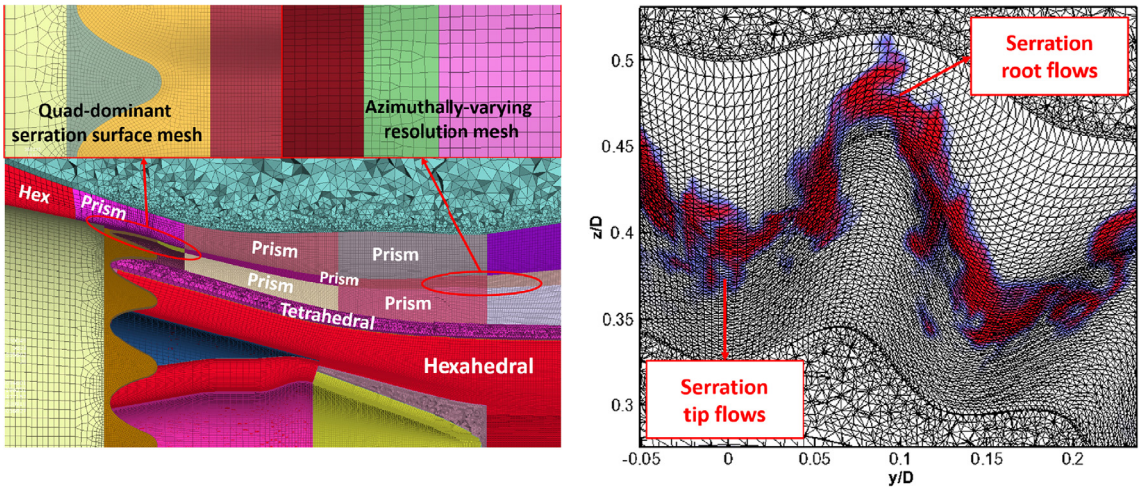

(a) Serration modular mesh topology (b) Serration shear layer

Fig. 3. Serrated nozzle shear layer and its modular mesh.

3.2. Serrated nozzle mesh strategy

Meshing the serrated bypass nozzle geometry is challenging due to its irregular nozzle shape. Serrations also generate azimuthally varying shear layers. To follow the serration-generated shear layers, a modular mesh strategy is used, implanting regions of unstructured mesh within the structured jet plume mesh. Fig. 3(a) shows the modular mesh topology for serration shear layers. The numerics are less dissipative on hexahedral meshes and thus hexahedrons are better for eddy resolving simulation [14]. The majority of the jet plume is meshed with hexahedral elements while the serrations and the shear layer are modelled using modular hybrid structured–unstructured meshes. This topology allows high-quality mesh to be generated locally near serrations and most importantly the azimuthal resolution can be adapted according to the smaller flow scales near the nozzle introduced by the serrations. The modular mesh sections are based on prism layers extruded from quad-dominant surface meshes. It produces a hexahedral dominant volume mesh. The mesh aligns with shear layer variations in the azimuthal direction, shown in Fig. 3(b).

Except for the modular section, the mesh used for the serrated nozzle is the same as that for the baseline round nozzle. Table 2 shows the grid statistics. There is around a 25% and 32% increase in node and edge number for the serrated nozzle mesh, which roughly corresponds to the simulation resolution and cost. These increases are caused by the serration-introduced smaller azimuthal structures near the nozzle that have to be resolved.

3.3. Far-field sound prediction

Far-field sound is predicted using the Ffowcs William–Hawkings (FW–H) equation from recorded flow time series on near-field surfaces. These surfaces are placed in the irrotational region to avoid hydrodynamic contamination of the acoustic

Table 2
Mesh statistics for baseline and serration jets ($N \times 10^6$).

	N_{node}	$N_{hexahedron}$	$N_{tetahedron}$	$N_{pyramid}$	N_{prism}	N_{cell}	N_{edge}
Baseline	32	29	16.8	0.22	0.032	46.2	107.6
Serration	40.2	34.7	30.5	0.57	0.38	66.2	141.7

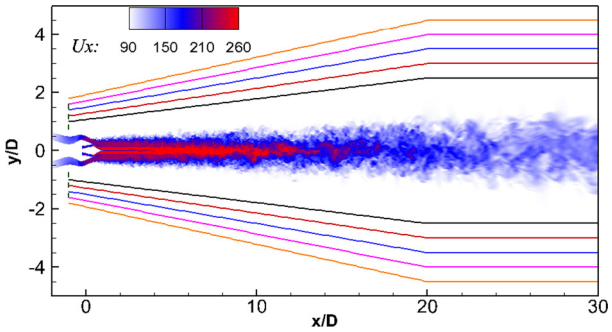

Fig. 4. FW–H integral surfaces near-field placement.

predictions. The approximate FW–H surface placement in the near field is shown in Fig. 4. The convective formula [21] is used for sound prediction because the jets are operating under a forward flight stream. The formula can be written as

$$4\pi\tilde{p}'(\mathbf{x},t) = \int_S [(1-M_0\tilde{R}_1)\frac{\dot{Q}_i n_i}{R^*} - U_0\frac{\tilde{R}_1^* Q_i n_i}{R^{*2}}]\,\mathrm{d}S + \int_S [\frac{\dot{L}_{ij} n_j \tilde{R}_i}{c_0 R^*} + \frac{L_{ij} n_j \tilde{R}_i^*}{R^{*2}}]\,\mathrm{d}S \tag{7}$$

where $\mathbf{x}$ is the observer's location and $\mathbf{y}$ is the source location. U_{0j} is the flight stream velocity in the x_j-direction. The mass flux is $Q_i = \rho U_i - \rho_0 U_{0i}$, the momentum flux is $L_{ij} = \rho u_i'(u_j' + U_{0j}) + p'\delta_{ij}$. The time derivative is expressed by $\dot{(*)} = \partial(*)/\partial t$, while the spatial derivative is expressed by $\tilde{(*)}_i = \partial(*)/\partial x_i$. The acoustic distance R^*, the flight stream factor β, and the radiation distance R are defined as

$$R^* = \sqrt{(x_1-y_1)^2 + \beta[(x_2-y_2)^2 + (x_3-y_3)^2]} \tag{8}$$

$$\beta = \sqrt{1-M_0^2} \tag{9}$$

$$R = \frac{-M_0(x_1-y_1) + R^*}{\beta^2} \tag{10}$$

4. Results

The validation of the methodology can be found in [11–14,17] and summarized in the appendix. In this section, the serration effects are discussed using LES data from perspectives of flow and acoustics. The sound sources are explored using fourth-order space–time correlations.

4.1. Flow field

Fig. 5 shows an overview of the LES results on flows and acoustics from serration nozzle. The relatively small turbulent structures introduced by the serrated nozzle are resolved by the current grid. The small hairpin vortex structures develop from the serration root and gradually grow into larger size downstream. This tends to increase turbulent mixing and also dissipates energy faster. The eddies are coloured by the radial velocity component. The flow from the serration root has larger radial velocity than that from the serration tip because of serration penetration. Downstream of the nozzle serrations, the serration root flow is moving outwards, while the serration tip flow is moving relatively inwards. This forms a pair of streamwise vortices downstream of each serration. Compared with round nozzle jets, the serrations break up the axi-symmetric azimuthal ring-like coherent structures into smaller-scale roll-up structures. This has the "calming effect" of reducing the overall turbulence, which is to be shown in the following paragraphs. This supports the hypothesis in [5] that the early break-up of the azimuthal structures near the nozzle helps to reduce the noise by decreasing the downstream turbulence level.

The serration-induced streamwise vortices break up the azimuthal coherent structures; they are better visualized in Fig. 6(a) using axial vorticity. The streamlines are also coloured by radial velocity. It shows that a pair of streamwise vortices

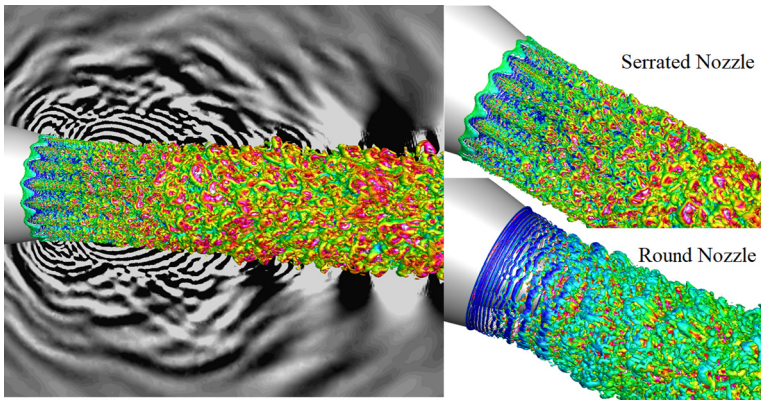

Fig. 5. Q-criterion coloured by radial velocity with $\frac{dp}{dt}$ indicating the acoustic field.

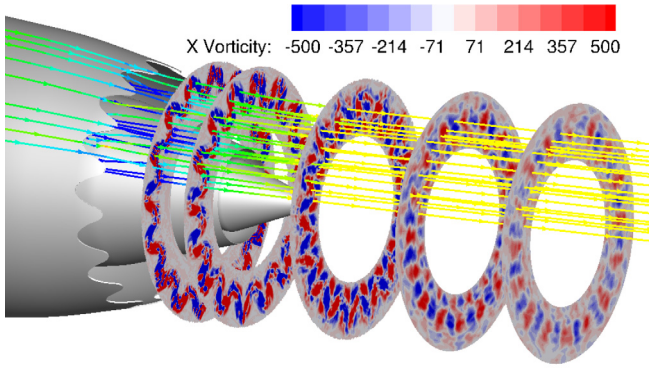

(a) Streamwise vortices

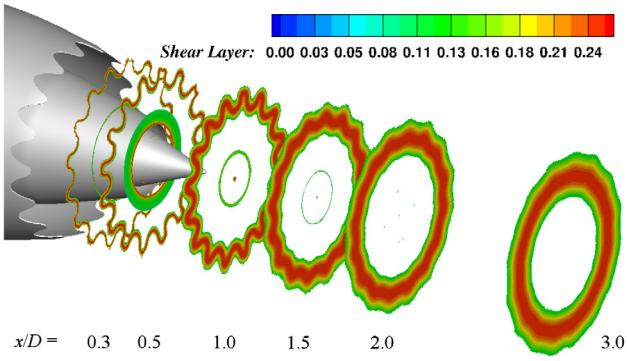

(b) Serrated nozzle shear layer

Fig. 6. Streamwise vortices and shear layer development for the serrated nozzle.

are generated by each serration near the nozzle. They further induce secondary vortices downstream, i.e. $x/D = 1$, which contributes to increased mixing and dissipation. These streamwise vortices are also dissipated quickly when being convected downstream. This is a result of the relatively smaller size of civil aeroengine serrations than the more aggressive serrations studied previously [13]. Thus the streamwise vorticity increased mixing is confined in the near-nozzle region. Another aspects of these streamwise vortices can be seen as azimuthal variation of shear layer; it is shown in Fig. 6(b).

For the time-mean flow field, Fig. 7 shows a direct comparison between the baseline and the serration jets. The jets are under the influence of a flight stream, so spreading is reduced radially. However, serration effects on flow velocity are still evident near the nozzle. The jet spreads rapidly at the serration roots and contracts at the tips. This causes the shear layer to vary periodically in the azimuthal direction and characterizes the initial development of serrated nozzle jets. As noted previously, the shear layer trajectory from the serrated nozzle is varied in the azimuthal direction (see Fig. 6(b)).

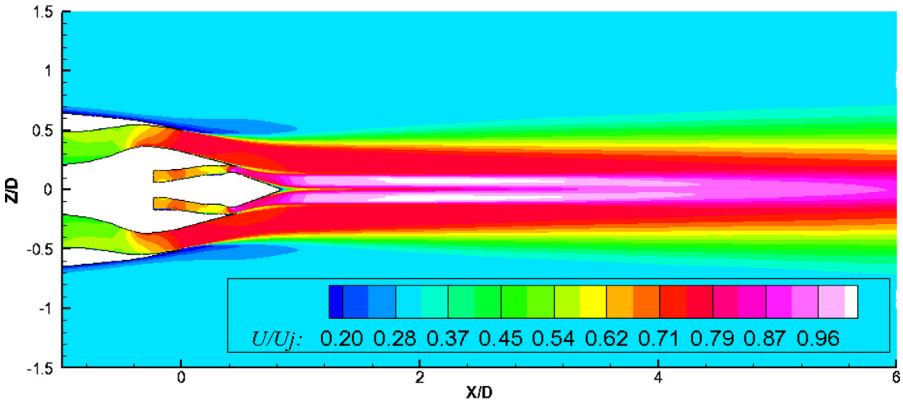

(a) Axial velocity for the baseline jet

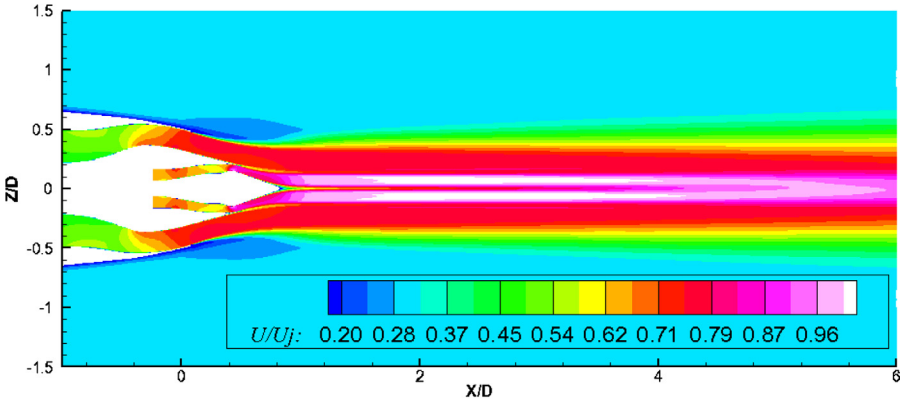

(b) Axial velocity at the serration tips

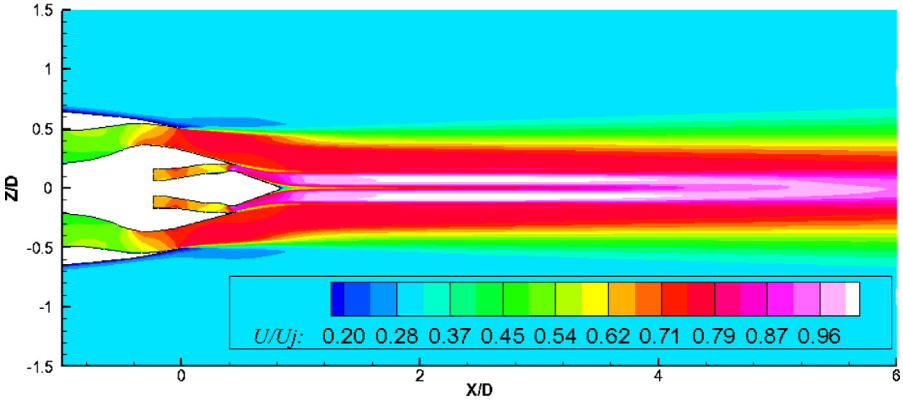

(c) Axial velocity at the serration roots

Fig. 7. Time-averaged velocity field for the baseline and serrated nozzle jets.

As for turbulent fluctuations in Fig. 8, serrations shrink the high-turbulence region and bring it closer to the nozzle. The turbulence for the serrated nozzle decays much faster than that for the baseline downstream. It indicates that serration-induced mixing increases the dissipation rate over that of the baseline. Looking at the turbulence distribution, the turbulence is generated differently at the tip and root. The turbulence at the root spreads more than that at the tip.

Since serration effects are close to the nozzle, radial profiles of velocity and turbulent fluctuations within $x/D = 1$ are further investigated. Fig. 9(a) shows the velocity development near the nozzle. As noted previously, the shear layer from the tip develops at lower radial locations, while that from the root is at higher radial locations. This difference is evident near the nozzle and gradually decreases as the jet develops downstream and spreads out radially. This increase the effective shear layer thickness. As for the turbulence development, the turbulent fluctuation profiles near the nozzle are shown in Fig. 9(b). The turbulence is initially intensified by serrations near the nozzle compared with the baseline. The peak from the

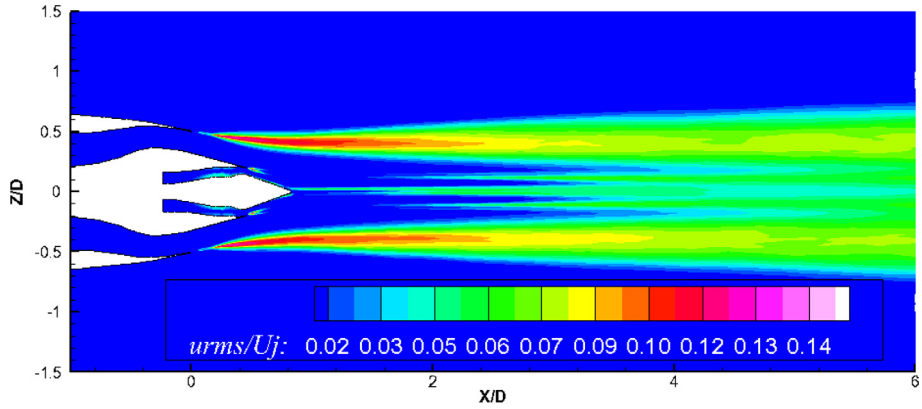

(a) Turbulent fluctuations for the baseline jet

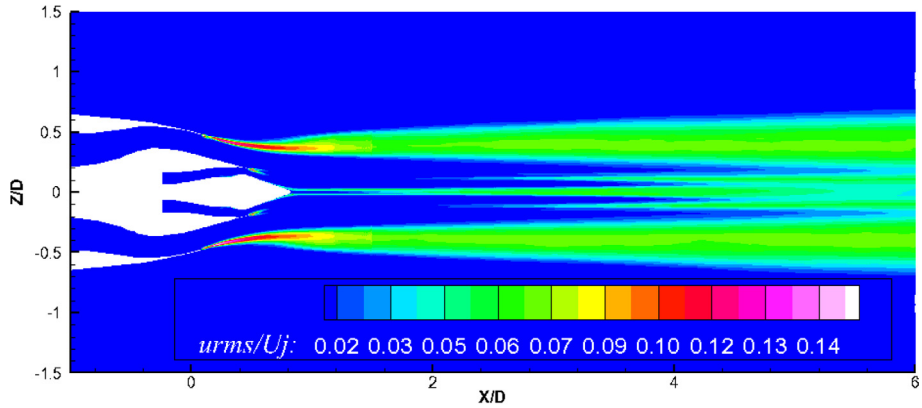

(b) Turbulent fluctuations at the serration tips

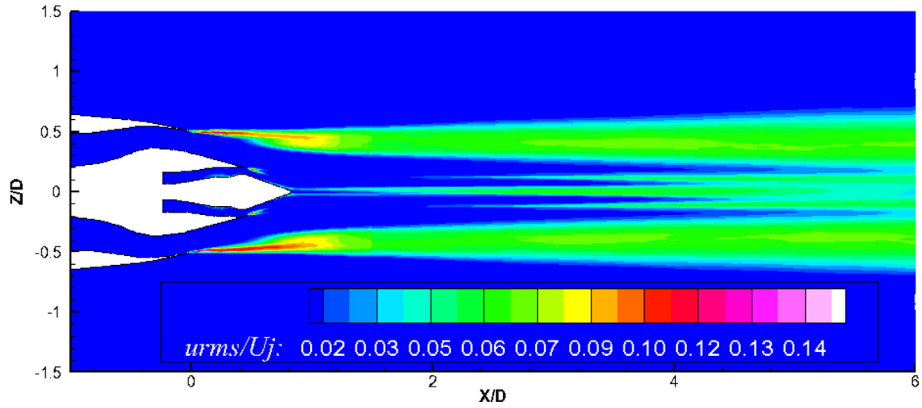

(c) Turbulent fluctuations at the serration roots

Fig. 8. Turbulent fluctuations for the baseline and serrated nozzle jets.

tip and root moves apart radially and gradually spreads out. The intensified peak decays fast as the energy is distributed more radially than the round jet.

Fig. 10(a) quantifies the mean radial locations of serration root and tip shear layer at different axial locations. This demonstrates the development of a shear layer azimuthal variation. The root shear layer is brought inwards by the flight stream, while the tip shear layer first contracts near the nozzle, then begins to spread after $x/D = 1$. The difference is taken between the root and tip and shown by the back line. The azimuthal difference first develops within $x/D = 0.5$, then plateaus until around $x/D = 1$. After that, turbulent mixing becomes dominant, and the azimuthal difference decreases rapidly. Finally, the jet becomes azimuthally homogeneous after $x/D = 4$.

The development of turbulent fluctuations following the shear layer and centreline is shown in Fig. 10(b). The serration-induced streamwise vortices increase mixing near the nozzle, so the turbulence in the shear layer decays sharply just

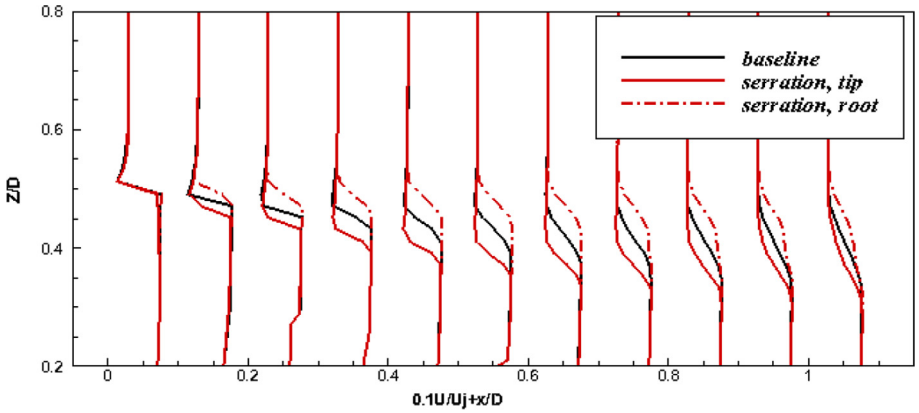

(a) Axial velocity

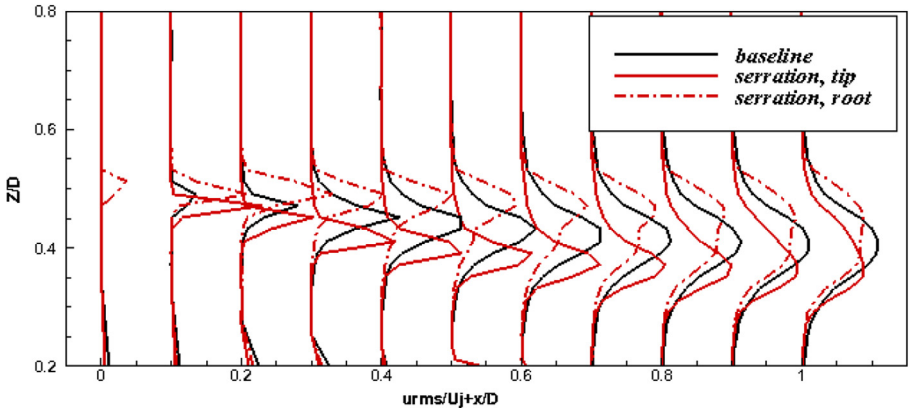

(b) Turbulent fluctuations

Fig. 9. Radial profiles of axial velocity and turbulent fluctuations for the baseline and serrated nozzle jets within $x/D = 1$.

downstream of the nozzle exit. The turbulence intensity is reduced to half of the initial level within two nozzle diameters downstream, while it takes around 12 diameters for the baseline round jets to reach this level. However, after $x/D = 2$, the serrated nozzle jet turbulence decreases gradually and finally the two jets decay to a similar level of turbulence far downstream at around $x/D = 15$. The centreline turbulence is also affected by the shear layer development. The first peak is caused by the interactions between outer bypass shear layer interactions with inner core jet shear layer, and the second is caused by bypass shear layer merging at the centreline. The first peak is intensified by serrations, and the second peak is delayed and reduced by the rapid decay of serration shear-layer turbulence.

4.2. Acoustics

An overview of the near-field acoustics is shown in Fig. 5. The acoustic waves are emitted by the sound sources near the nozzle and interfere with each other. As the Goldstein analogy source [22,23] is based on fourth-order space–time correlations, they are used here to inform near-field jet noise sources. They are calculated by performing correlations between two Reynolds stress tensors, so expressed in a fourth-order tensor:

$$R_{ijkl}(\vec{x}, \delta\vec{x}, \delta\tau) = \left\langle \left(\rho u_i' u_j' - \langle \rho u_i' u_j' \rangle\right)(\vec{x}, t) \cdot \left(\rho u_k' u_l' - \langle \rho u_k' u_l' \rangle\right)(\vec{x} + \delta\vec{x}, t + \tau) \right\rangle \tag{11}$$

The far-field sound can be obtained by integrating the correlations R_{ijkl} with the propagation Green functions in the source-containing region [23]. Therefore, the space–time correlations are interpreted physically as the sound sources that exhibit Gaussian distributions with turbulence temporal and spatial scales. The amplitude of the fourth-order correlation $R_{ijkl}(\vec{x}, 0, 0)$ represents the magnitude of the sound source. As the latter is mainly located inside shear layers, two representative axial locations $x/D = 1$ and 10 are picked along the shear layers to show the sound source characteristics for both the round and serrated nozzle jets. (See Fig. 11.) $x/D = 1$ is near the nozzle, where turbulence is triggered by the Kevin–Helmholtz instability, and $x/D = 10$ is around the potential core end where the outer shear layers merge at the centre line. Over these two representative locations, there are some major components that prominently contribute to the sound sources. The dominant sound source component is R_{1111} (axial), while the secondary largest components are R_{2222} (radial)

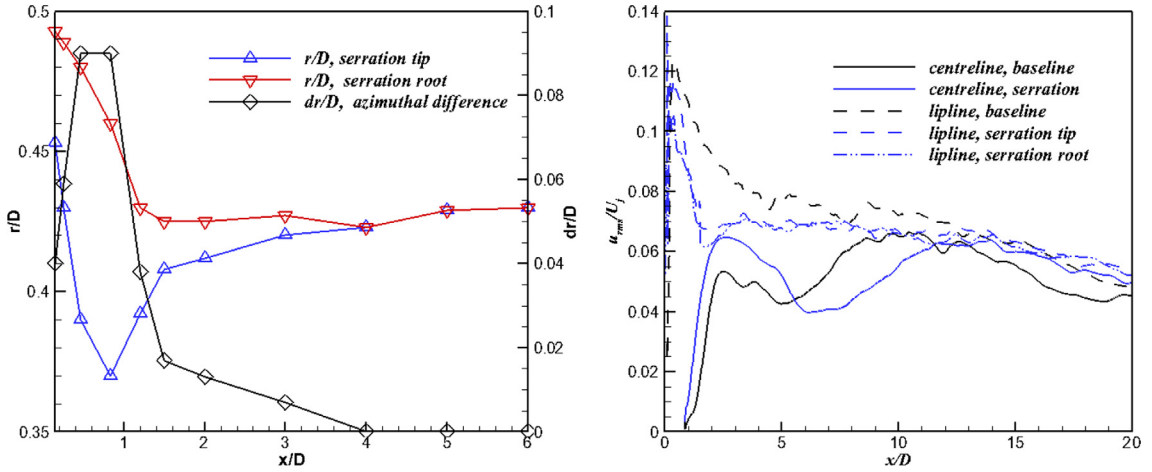

(a) Shear layer azimuthal difference (b) Shear layer turbulent fluctuations

Fig. 10. Shear layer development of azimuthal difference and turbulence fluctuations.

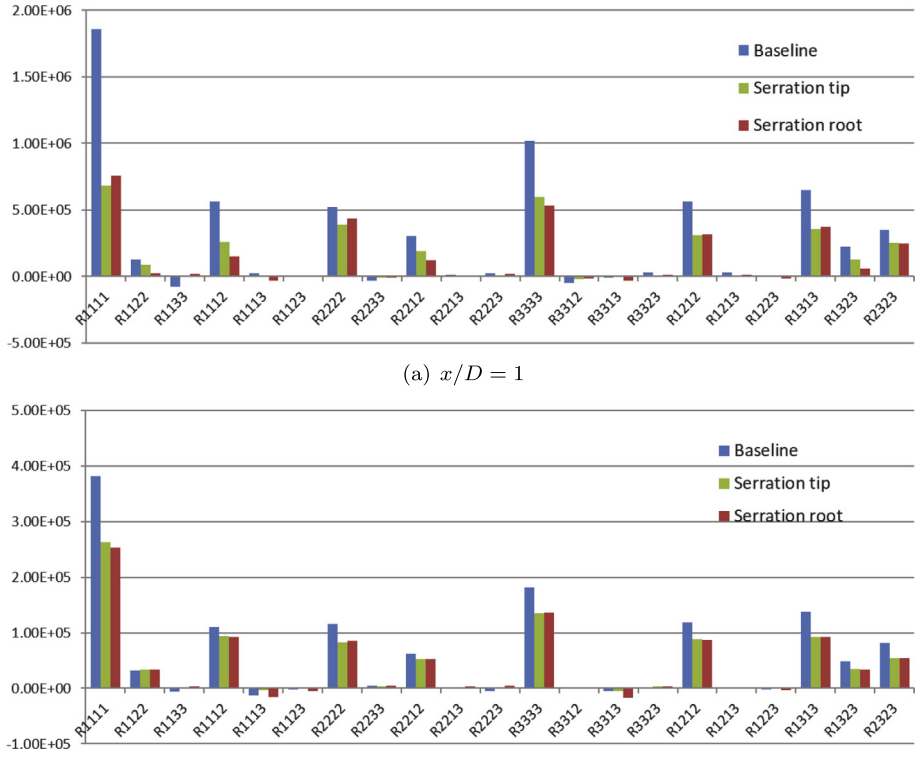

(a) $x/D = 1$

(b) $x/D = 10$

Fig. 11. Fourth-order correlation amplitudes in the shear layer ($kg^2/(m^2\,s^4)$).

and R_{3333} (azimuthal). The remaining major components are shear stress correlations, R_{1212}, R_{1313}, R_{2323}, R_{1112}, R_{2212} and R_{1323}, which indicates the interactions between velocity components. In addition to what was observed by Karabasov et al. [23], R_{1112}, R_{2212}, and R_{1323} are the new non-negligible terms associated with axial–radial and axial–radial–azimuthal velocity interactions in these UHBPR nozzle jets.

In the near-nozzle region ($x/D = 1$), serrations can dramatically reduce the major sound source components near the nozzle, and the reduction level at the serration tip and root is similar. The maximum reduction is seen on R_{1111} and then on R_{3333} and R_{1313}. This indicates that serrations have effects on reducing axial and azimuthal fluctuations. Moving downstream of the shear layer, the serration effect on source reduction becomes weaker at $x/D = 10$. Except on relatively

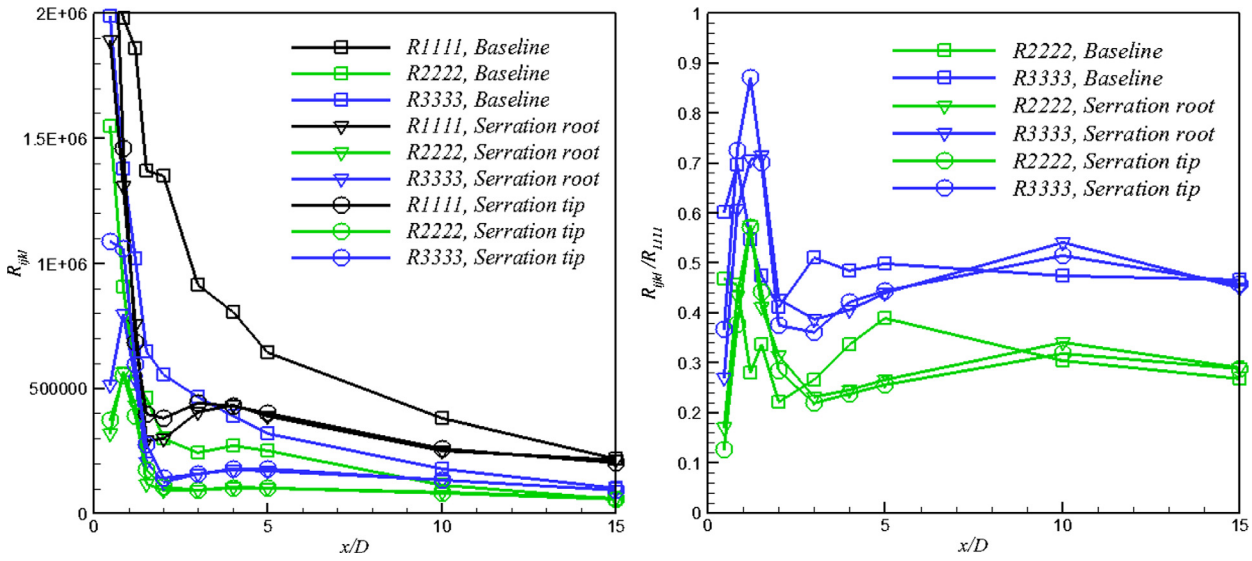

(a) R_{ijkl} amplitude $(kg^2/(m^2s^4))$ (b) R_{ijkl} amplitude relative to R_{1111}

Fig. 12. Fourth-order correlation amplitudes variation in the axial direction.

large magnitude reduction on axial component R_{1111}, the reduction on other source components are benign. This indicates that the serration effects on sound source are more pronounced near the nozzle.

To understand this more comprehensively, the variation of the three major sound source components is plotted along the shear layers at different axial locations in Fig. 12. Fig. 12(a) shows the absolute sound source amplitude up to axial distance of 15 D. The serrations make the sound source decay much faster compared to the baseline round jet. The source magnitude is rapidly reduced to a relatively low level before $x/D = 2$, while it takes 5–10 D for the baseline jet to achieve this. At around $x/D = 15$, all the three major sound source components R_{1111}, R_{2222}, and R_{3333} get to the same level as those of the baseline nozzle jet. This indicates that the serrations shorten the strong sound-source-containing region. In addition to this, the two components R_{2222} and R_{3333} develop differently from the baseline round jet near the nozzle. They are first intensified and exhibit a peak around $x/D = 1$, which might be related to the serration-introduced streamwise vortices. After this, they decay rapidly as R_{1111} does due to enhanced mixing. After normalization by the dominant component R_{1111}, the relative amplitudes of the other two source components, R_{2222} and R_{3333} are shown in Fig. 12(b). The relative amplitude is at similar levels for the two jets, except that the baseline round jet shows slightly higher values around $x/D = 5$.

Far-field sound spectra as shown in Fig. 13 have been calculated based on near-field FWH surface integrals. The 1/3 octave spectra is plotted with narrow spectra to better illustrate the trend. The Strouhal number ($St = \frac{f D_{\text{bypass}}}{U_{\text{core}}}$ that the current grid can resolve is up to around 2.4. The extrapolation has been made at the St limit by using the 1/3 octave spectra slope to show the spectra trend in the high-frequency range. The serrations tend to shift the acoustic energy from low to high frequencies. The spectra are about to cross at around $St = 3$ for 30°, while this occurs above $St = 4$ for 120°. This is consistent with what was observed in the existing chevron design [2,5].

As a series of surfaces with increasing radial position were placed in the near field, the sensitivity of far-field sound prediction to the surface locations is checked in Fig. 14(a). It shows a convergent prediction of far-field sound from all surfaces, the maximum discrepancy among these surfaces is within 1.5 dB. It has been shown that serrations can reduce noise over a range of low frequencies for this UHBPR jet. Although the trend of the increased sound pressure level at high frequencies is demonstrated by extrapolating the spectra at the current resolved St limit, the high-frequency penalties are not directly evaluated in the overall sound pressure level (OASPL). Accordingly, OASPL is obtained by integrating the spectra from $St = 0.06$ to 2.4, considering only low-frequency noise reduction. Fig. 14(b) shows the comparison of OASPL between the baseline round and the serration jets. The serrations reduce the overall far-field sound level by 2–4 dB in the low-frequency range. When high frequency penalties are considered, the overall noise reduction might be reduced at high polar angles. This is to be confirmed in the future study by using a refined mesh to resolve larger frequency ranges.

5. Conclusions

High-resolution LES is performed for complex geometry UHBPR jets with and without serrations. Non-dissipative numerics are utilised employing a KEP scheme with fourth-order smoothing, allowing modular hybrid structured–unstructured meshes to be used. A mixed non-linear SGS model is used in the LES region and hybridized with the SA RANS to model boundary layers on the nozzle. The shear layer from the serrated nozzle is inhomogeneous azimuthally, so a modular hybrid mesh is used to follow the serrated nozzle shear layer, facilitating mesh generation and also increasing mesh quality.

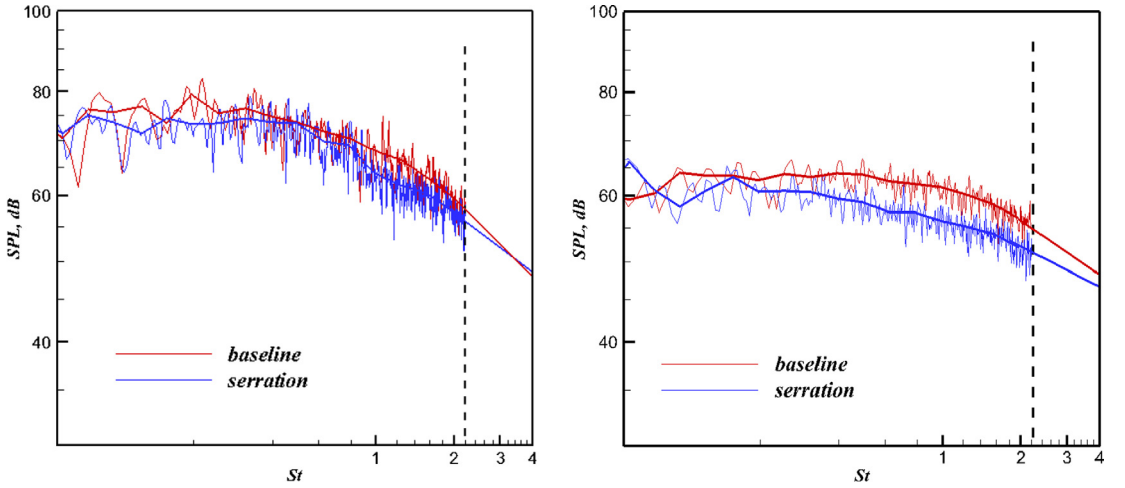

(a) Sound spectra at 30° polar angle (b) Sound spectra at 120° polar angle

Fig. 13. Far-field sound spectra prediction.

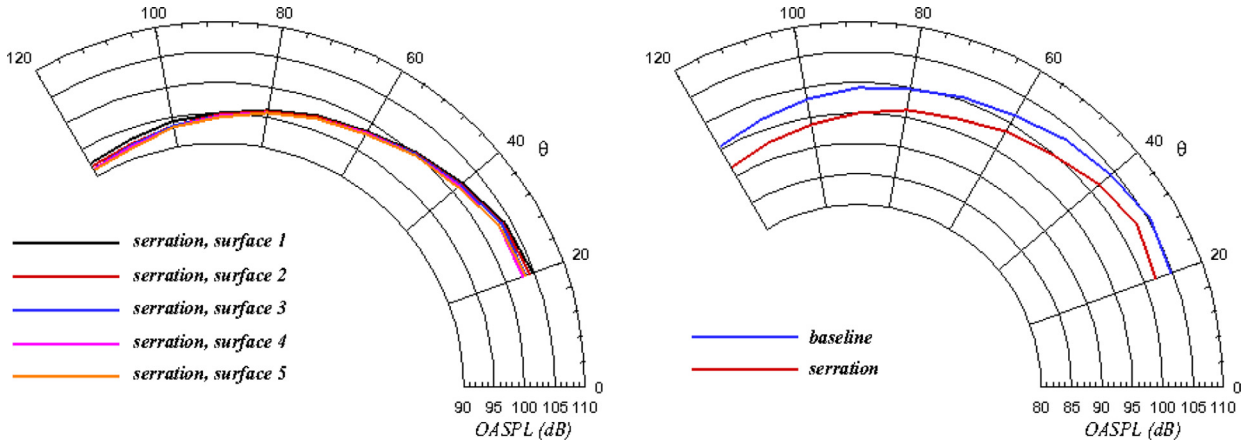

(a) OASPL prediction on all FW–H surfaces (b) OASPL for the baseline and serration jets

Fig. 14. Overall sound pressure level (OASPL) integrated over the frequency range ($St = 0.06 - 2.4$).

The results show that serration effects are evident near the nozzle for both mean flow velocity and turbulent fluctuations. The flow spreads rapidly from serration roots and contracts from the tips. This forms streamwise vortices and induces shear layer azimuthal variation. The azimuthal variation develops in the first $1D$ downstream, then decays quickly when the mixing becomes dominant. The serrated nozzle jet finally returns to a round jet at $x = 4D$. The streamwise vortices thicken the shear layer and introduce small-scale turbulence near the nozzle. Therefore, the turbulent fluctuations are intensified in the nozzle exit region and dissipated rapidly to half of the initial level by $x = 2D$ due to enhanced mixing. Turbulent fluctuations for the serrated nozzle jet remain lower than the round jet until $x = 15\,D$. For the serrated nozzle, the extent of the high-turbulence region is reduced and moves upstream.

The near-field sound source is indicated by fourth-order space–time correlations based on Goldstein's acoustic analogy. The major source components are R_{1111}, R_{2222}, R_{3333}, R_{1212}, R_{1313}, R_{2323}, R_{1112}, R_{2212}, and R_{1323}. Among them, R_{1111} dominates and is followed by R_{2222} and R_{3333}. R_{1112}, R_{2212}, and R_{1323} are the new non-small axial–radial and axial–radial–azimuthal interaction components of the sound sources in these UHBPR jets compared with the previous single stream round jets [23]. The serrations dramatically reduce the amplitude of the major sound sources. As also reflected by the turbulence levels, the serrated nozzle sound sources decay rapidly near the nozzle and remain at a lower level than the baseline from $x = 2\,D$ to $15\,D$. This makes sound sources more concentrated near the serrated nozzle exit and shortens the high-intensity-source-containing region.

Based on the near-field surface data, the convective FW–H formula is used to predict farfield sound for the UHPBR jet subject to a forward flight stream. LES along with FW–H integration displays a convergent far-field sound prediction. It shows that the serrations reduce noise in the low frequencies. The OASPL in the far field has been reduced by 2–4 dB for the serrated nozzle jet when integrating low-frequency sound up to $St = 2.4$. In the future, this LES data could be used to

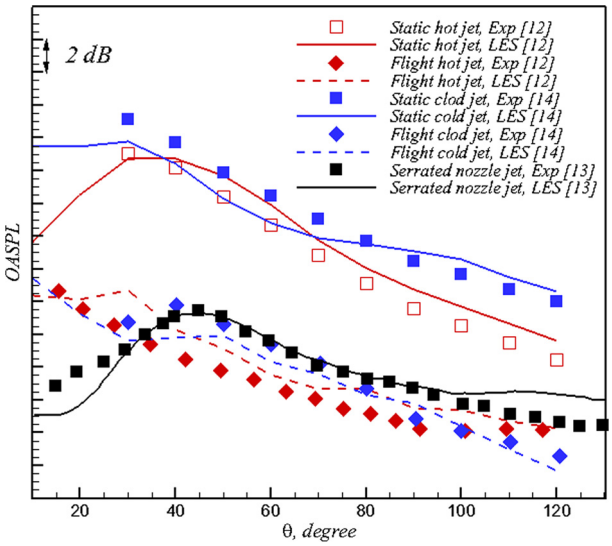

Fig. 15. Summary of the validated jet noise prediction.

complement or replace data from experiments and aid the development of noise reductions strategies in the aspects of cost and data richness.

Acknowledgements

The work is performed under the EU 7th Framework Programme-funded project "JERONIMO" (ACP2-GA-2012-314692-JERONIMO) and the ARCHER computing time provided by the UK Turbulence Consortium under EPSRC grant EP/L000261/1. The fruitful discussions with Dr. Peer Boehning from Rolls-Royce Deutschland are also greatly acknowledged.

Appendix A. Methodology validation

The simulation methods used in this paper has been validated vastly in previous researches [11–14,17]. The typical results are summarized in Fig. 15. They include far-field sound level predictions of five jets compared with experimental measurement. The nozzle covers round and serrated shapes and the operating conditions cover the hot and cold jets with and without flight stream. The discrepancy between the predicted and measured value is less than 2 dB. More details about the validation can be found in the published papers mentioned above.

References

[1] M.J. Lighthill, On sound generated aerodynamically: I. General theory, Proc. R. Soc. Lond. A 211 (1952) 564–587.
[2] S. Martens, Jet noise reduction technology development at GE aircraft engines, in: ICAS 2002 Congress Paper, 842.
[3] P. Jordan, T. Colonius, Wave packets and turbulent jet noise, Annu. Rev. Fluid Mech. 45 (2013) 173–195.
[4] M.B. Alkistar, A. Krothapalli, G.W. Bulter, The effect of streamwise vortices on the aeroacoustics of a Mach 0.9 jet, J. Fluid Mech. 578 (2007) 139–169.
[5] K.B.M.Q. Zaman, J.E. Bridges, D.L. Huff, Evolution from tabs to chevron technology: a review, Int. J. Aeroacoust. 10 (2011) 685–710.
[6] C.E. Tinney, P. Jordan, The near pressure field of coaxial subsonic jets, J. Fluid Mech. 611 (2008) 175–204.
[7] V.G. Mengle, R. Elkoby, L. Brusniak, Reducing propulsion airframe aeroacoustic interactions with uniquely tailored chevrons: 1. Isolated nozzle, AIAA Paper 2006–2433.
[8] V.G. Mengle, R. Elkoby, L. Brusniak, Reducing propulsion airframe aeroacoustic interactions with uniquely tailored chevrons: 2. Installed nozzle, AIAA Paper 2007–2434.
[9] V.G. Mengle, R. Stoker, L. Brusniak, R. Elkoby, Flapron modification effect on jet-flap interaction noise reduction for chevron nozzles, AIAA Paper 2007–3666.
[10] M.L. Shur, P.R. Spalart, M.K. Strelets, A.K. Travin, Towards the prediction of noise from jet engines, Int. J. Heat Fluid Flow 24 (2003) 551–561.
[11] Z.-N. Wang, I.Z. Naqavi, M. Mahak, P. Tucker, X. Yuan, P. Strange, Far field noise prediction for subsonic hot and cold jets using large-eddy simulation, in: ASME Paper GT2014-27290.
[12] Z.-N. Wang, I.Z. Naqavi, M. Mahak, P.G. Tucker, P. Boehning, Large-eddy simulation of the flight stream effects on single stream heated jets, AIAA Paper 2017–0457.
[13] H. Xia, P.G. Tucker, Numerical simulation of single-stream jets from a serrated nozzle, Flow Turbul. Combust. 88 (2012) 3–18.
[14] J. Tyacke, I. Naqavi, Z.-N. Wang, P.G. Tucker, P. Boehning, Predictive LES for jet aeroacoustics: current approach and industrial application, J. Turbomach. 139 (2017) 081003, https://doi.org/10.1115/1.4035662.
[15] J.C. Tyacke, Z.-N. Wang, P.G. Tucker, LES-RANS of installed ultra-high bypass-ratio coaxial jet aeroacoustics with a finite span wing-flap geometry and flight stream – part 1: round nozzle, AIAA Paper 2017–3854.
[16] A. Jameson, Formulation of kinetic energy preserving conservative schemes for gas dynamics and direct numerical simulation of one-dimensional viscous compressible flow in a shock tube using entropy and kinetic energy preserving schemes, J. Sci. Comput. 34 (2008) 188–208.

[17] Z.-N. Wang, J. Tyacke, P. Tucker, Hybrid LES/RANS predictions of flows and acoustics from an ultra-highbypass-ratio serrated nozzle, in: Note on Numerical Fluid Mechanics and Multidisciplinary Design: Progress in Hybrid RANS-LES Modeling, 2018, pp. 1–12, in press.
[18] P. Tucker, Differential equation-based wall distance computation for DES and RANS, J. Comput. Phys. 190 (1) (2003) 229–248, https://doi.org/10.1016/S0021-9991(03)00272-9.
[19] P.R. Spalart, S.R. Allmaras, A one-equation turbulence model for aerodynamic flows, Rech. Aérosp. 1 (1994) 5–21.
[20] Y. Liu, P.G. Tucker, R.M. Kerr, Linear and nonlinear model large-eddy simulations of a plane jet, Comput. Fluids 37 (2008) 439–449.
[21] A. Najafi-Yazdi, G.A. Bres, L. Mongeau, An acoustic analogy formulation for moving sources in uniformly moving media, Proc. R. Soc. Lond. A, https://doi.org/10.1098/rspa.2010.0172.
[22] M.E. Goldstein, A generalized acoustic analogy, J. Fluid Mech. 488 (2003) 315–333.
[23] S. Karabasov, M. Afsar, T. Hynes, A. Dowling, W. McMullan, C. Pokora, G. Page, J. McGuirk, Jet noise: acoustic analogy informed by large eddy simulation, AIAA J. 48 (7) (2010) 1312.